Brain folding is initiated by mechanical constraints without a cellular pre-pattern

Andrew K Lawton[1], Tyler Engstrom[2], Daniel Rohrbach[3], Masaaki Omura[3,4,5], Daniel H Turnbull[4], Jonathan Mamou[3], Teng Zhang[6], J. M. Schwarz[2], and Alexandra L Joyner[1,7,*]

[1] Developmental Biology Program. Sloan Kettering Institute. New York, NY 10065. USA.

[2] Department of Physics, Syracuse University, Syracuse, NY 13244, USA

[3] Lizzi Center for Biomedical Engineering, Riverside Research, NY

[4] Skirball Institute of Biomolecular Medicine and Department of Radiology, NYU School of Medicine, NY 10016, USA

[5] Graduate School of Science and Engineering, Chiba University, Chiba 263-8522, Japan

[6] Department of Mechanical & Aerospace Engineering, Syracuse University, Syracuse, NY 13244, USA

[7] Biochemistry, Cell and Molecular Biology Program, Weill Graduate School of Medical Sciences of Cornell University, New York, NY, 10065

[*] Corresponding author: joynera@mskcc.org

Summary

During human brain development the cerebellum and cerebral cortex fold into robust patterns that increase and compartmentalize neural circuits. Although differential expansion of elastic materials has been proposed to explain brain folding, the cellular and physical processes responsible at the time of folding have not been defined. Here we used the murine cerebellum, with 8-10 folds, as a tractable model to study brain folding. At folding initiation we considered the cerebellum as a bilayer system with a fluid-like outer layer of proliferating precursors and an incompressible core. We discovered that there is no obvious cellular pre-pattern for folding, since when folding initiates, the precursors within the outer layer have uniform sizes, shapes and proliferation, as well as a distribution of glial fibers. Furthermore, although differential expansion is created by the outer layer expanding faster than the core at folding initiation, thickness variations arise in the outer layer that are inconsistent with elastic material models. A multiphase model was applied that includes radial and circumferential tension and mechanical constraints derived from *in vivo* measurements. Our results demonstrate that cerebellar folding emerges from mechanical forces generated by uniform cell behaviors. We discuss how our findings apply to human cerebral cortex folding.

Introduction

Recent work in brain folding has primarily focused on the cerebral cortex and involved models of differential expansion of elastic materials to drive mechanical instabilities that lead to folding[1-7]. Current models are able to create three dimensional shapes strikingly similar to the folds seen in the human cortex[8]. However, the cell and tissue level mechanics actually present at the initiation of folding have not been considered or defined. The simple alignment of folds along the anterior-posterior axis of the murine cerebellum and the genetic tools available in mouse allow for precise developmental interrogation, to identify and analyze the cellular behaviors driving growth that could create differential expansion, and to reveal additional critical forces.

The developing cerebellum is distinct from the cerebral cortex, as it has an external granule cell layer (EGL) of proliferating precursors that covers the surface and generates growth primary in the anterior-posterior (AP) direction[9-11]. A bilayer system is therefore an excellent starting approximation for cerebellar folding. Here we show that cerebellar folding emerges from differential expansion between an un-patterned uniformly expanding fluid-like EGL and an incompressible underlying core. Additionally, we demonstrate that thickness variation in the EGL at the base of the forming fissures, termed anchoring centers (AC)[12], are inconsistent with traditional elastic wrinkling models driven by differential growth. We constrained a recent model[13] that takes into consideration that tension could play an import role in the developing brain and used our in depth developmental data to capture the initiation of cerebellar folding.

No cellular pre-pattern at initiation of folding

To systematically determine the cellular behaviors underlying the initiation of cerebellar folding, we first tested whether regional differences in EGL proliferation rates are present that could influence the folding pattern of the cerebellum, since the EGL drives the majority of cerebellar growth[9-11]. Proliferation rates (S phase index) were measured in the EGL during folding initiation (E16.5 and E17.5) in the inbred FVB/N strain to reduce variation between samples. First we asked if the regions that will give rise to distinct sets

of lobules have different rates of proliferation that could contribute to the larger and smaller sizes that the lobules ultimately attain. We focused on the anterior cerebellum that divides into a larger region with lobules 1-3 (L123) and smaller region (L45), as well as the central area that comprises lobules 6-8 (L678) of the cerebellum (Figure 1a-b). The more posterior cerebellum does not consistently fold at this stage, thus measurements were not included. Interestingly, we found that the proliferation rates were the same in the three regions at E16.5 (Fig. 1c). The EGL proliferation rate in L678 was slightly reduced compared to the L123 region at E17.5, but no other differences were found (Fig. 1d). Thus proliferation is uniform just before initiation of folding and the small difference found during folding does not correlate with lobule size. This result indicates that lobule size is not determined by modulating the levels of proliferation at the onset of folding. Rather, lobule size could be set by the timing of invagination and the distance between ACs as granule cell precursors do not cross ACs [10].

Each AC is first detected by a regional inward thickening of the EGL[12]. We measured the proliferation of the EGL specifically within the forming AC regions to test whether altered proliferation rates could explain the thickenings and therefore the initiation of an AC. We found the rate of proliferation within each forming AC region at E16.5 and E17.5 was the same as in the surrounding EGL (Fig. 1e,f), thus proliferation within all regions of the EGL at the initiation of folding is uniform. Furthermore, regional modulation of proliferation does not form or position the ACs.

At E18.5, after the initiation of folding, we found that the rate of proliferation was significantly lower in the L678 region compared with the L123 and L45 regions (Supplemental Fig. 1a). However, proliferation within the ACs at E18.5 remained uniform with the surrounding regions (Supplemental Fig. 1b). Therefore, as ACs compartmentalize the EGL, regional differences in proliferation rates can arise in lobule regions, which thus could be important for determining the ultimate shapes of the folds.

Changes in cell size and shape have been shown to induce morphological changes[14-17]. To test if regionally specific regulation in cell shape or size directs folding, we fluorescently labeled cell membranes of scattered granule cell precursors (GCPs) in the EGL using genetics (*Atoh1-CreER/+; R26*$^{MTMG/+}$ mice injected with tamoxifen two days prior to analysis). We then segmented the cells in 3D and quantified their sphericity (Fig. 1g). We discovered that GCPs in the EGL take on a large variation of shapes and sizes at E16.5 and E18.5. However, we found no difference in cell shape in the different lobule regions of the EGL or between the AC areas and the surrounding EGL at either age (Fig. 1h,i). Cell size was uniform at both stages except for a slight reduction in L678 at E16.5 when compared with L123 and the AC regions. However, cell size is reduced at E18.5 (Fig 1 j,k and Supplemental Fig. 1c). Thus, the proliferating GCPs that drive expansion of the EGL have similar shapes and sizes across the lobule regions defined by the first three ACs at folding initiation.

The EGL is traversed by fibers of Bergmann glial and radial glial cells[18-20]. We tested whether the fibers are distributed in patterns that could locally change the physical properties of the EGL and induce invaginations. Genetics was used to fluorescently label cell membranes of scattered glial cells (*nestin-creER/+;R26*$^{MTMG/+}$ mice injected with tamoxifen at E14.5) (Fig 2a). Fibers crossing the EGL at E16.5 were counted in sagittal slices and aligned relative to the ACs (Fig. 2b). This analysis showed that the Bergmann glial and radial glial fibers are distributed evenly along the AP axis of the EGL, and therefore are not directing the positions where folding initiates based on an uneven regional distribution.

Taken together, our results show that at the initiation of folding, the EGL has uniform cell behaviors and distribution of glial fibers, and thus has no evidence of any pre-patterning in the EGL. Other factors therefore must be guiding cerebellar folding. We chose to test whether there is an emergent tissue-level regulation of folding.

Tissue level mechanical forces drive folding

107 It is well known that differentially expanding bilayer systems can wrinkle to relax building stress[21-25]. We
108 reasoned that in the cerebellum the EGL could behave as a quickly expanding outer layer and its
109 attachment to a more slowly growing core could generate forces that result in a wrinkling-like phenotype.
110 To test whether the cerebellum has differential expansion between the two layers, we measured the
111 expansion of the EGL and the core during the time of initiation of folding from midline sagittal sections
112 (Fig 3a-d). The length of the surface of the EGL was used as a measure of the cerebellum surface area and
113 the area of the core as an approximation of cerebellum volume (Fig. 3d), and measurements were made
114 each day from E16.5 through P0. In cross-section the unfolded cerebellum approximates a semicircle,
115 therefore we reasoned that if the cerebellum were to remain unfolded then the ratio of expansion between
116 the length of the EGL and the area of the core should approximate the ratio of the circumference of a
117 semi-circle to its area. Of significance, we found that at E16.5 and E17.5 the ratios of growth between the
118 EGL and core closely approximated the expansion of a semi-circle. However, at E18.5 and P0 the
119 expansion rate of the EGL was greater than the rate of core expansion (Fig. 3e). Thus we uncovered that
120 the cerebellum does indeed go through a phase of differential expansion. We next determined whether
121 differential expansion correlates with folding by calculating a folding index (the convex curvature of the
122 EGL divided by the length of the EGL) at each stage[26]. Indeed, we found that the cerebellum remains
123 unfolded during the initial proportional expansion between the EGL and core and only folds when the
124 differential expansion is initiated (Fig. 3f). These results provide physical evidence that cerebellar folding
125 is derived from tissue level mechanical forces arising from differential expansion.
126
127 **Elastic bilayer models do not account for shape change**
128 Since cerebellar folding correlates with differential expansion, we tested an elastic bilayer model against
129 our data for how the EGL grows faster than the core[22]. The resulting wrinkling instability should set up a
130 characteristic lengthscale of the distance between folds as the initial sinusoidal undulations increase in
131 amplitude to ultimately turn into lobules. The folding wavelength will depend on the thickness of the
132 external layer (EGL) and the ratio of the stiffness of the two layers (EGL/core). In particular, for a planar

133 geometry, with the stiffness of the external layer defined as E_o, the stiffness of the core as E_i, and the
134 thickness of the external layer denoted as t, the folding wavelength λ is given by[27]

$$\lambda = 2\,\pi\,t\,\left(\frac{1}{3}\frac{E_o}{E_i}\right)^{1/3}.$$

135 If the length of the system is l, then the number of folds is

$$n = \frac{l}{\lambda} \propto \frac{l}{t}\left(\frac{E_i}{E_o}\right)^{1/3}.$$

136 In other words, the number of folds is inversely proportional to the thickness of the EGL.

137

138 To more closely model the geometry of the cerebellum, we explored a standard elastic bilayer model in a
139 circular geometry using the observed ratio of thickness of the EGL to radius of the cerebellum near the
140 onset of shape change (smooth to wrinkled after E16.5) and invoking a neo-Hookian elastic solid for both
141 layers[28]. Previous work applied a tri-layer elastic model to the cerebellum, incorporating the molecular
142 layer[7]. We have not included the molecular layer in our model since it is not present when folding
143 initiates. The resulting shape change was studied as a function of the ratio of the layer stiffness values
144 (Fig. 4a). We found that to induce the observed number of folds at initiation of folding through wrinkling
145 based models constrained by our measurements of the embryonic cerebellum, a large stiffness ratio was
146 required of around 50. To map the stiffness contrast in the cerebellum we used scanning acoustic
147 microscopy to measure the bulk modulus of the cerebellum daily from E16.5 to P18.5 (Fig. 4b-c,
148 Supplemental Fig. 2). For small deformations, we expect the instantaneous bulk modulus to be linearly
149 related to the stiffness and, therefore, the ratio of the instantaneous bulk moduli should scale similarly to
150 the ratio of stiffnesses (assuming the same Poisson's ratio). We found that although the EGL has a higher
151 instantaneous bulk modulus than the core at all stages measured, the ratio was not sufficient to produce a
152 folding wavelength similar to that in the cerebellum (Fig. 4d). Small modulus contrasts have been
153 reported for other brain regions with other test modes.[29]

154

155 Wrinkling models predict compressive forces in the outer layer. Consistent with this prediction,
156 simulations of cuts through the outer layer and into the inner layer predict that the outer layer should not
157 open (Fig. 4e). Using surgical dissection blades we made radial cuts across the meninges, EGL, and into
158 the core of live E16.5 tissue slices. Time-lapse imaging revealed that unlike the prediction, the EGL opens
159 as well as part of the underlying cut in the core (Fig. 4f-h, Supplemental Fig. 4a-c, and Supplemental
160 Movie 1). This result is consistent with there being circumferential tension within the outer layers of the
161 cerebellum.
162
163 An additional aspect of the model that does not fit the biology of the developing cerebellum is that it
164 requires the EGL to be thinnest at the base of each AC, which are the lowest parts of the cerebellar
165 surface, and thus to have an "in-phase" thickness variation[13]. Without this feature, a purely elastic model
166 cannot be in mechanical equilibrium (in the quasistatic limit). However, we previously noted that the EGL
167 is thickest in the ACs when folding initiates, i.e., it has an "out-of-phase" thickness variation[12]. To
168 validate this observation, we quantified the thickness of the EGL and found it to be around 1.2 – 1.4 times
169 thicker in the ACs than in the surrounding EGL at E16.5 and 17.5 when folding initiates (Fig. 5a-d and
170 Supplemental Fig. 3), and the thickness ratio increased to 1.7 times at E18.5 (Fig 5d). It is of interest to
171 note that the final thicknesses of the layers of the cortex of the mature cerebellum, just as in the cerebral
172 cortex, are in-phase. These results further show that traditional wrinkling models cannot capture the
173 initiation of cerebellum folding, and highlight the importance of making measurements at the time of
174 folding rather than when it is complete.
175
176 **A multiphase model approximates folding**
177 We recently developed a model for folding from differentially expanding bi-layer brain tissues that takes
178 into account the possible contribution of mechanical constraints present in the developing brain[13]. We
179 made five primary assumptions based on the measurements presented above. First, the core is an
180 incompressible material (μ), as indicated by our instantaneous bulk modulus measurements. Second we

utilize a uniform expansion of the EGL (k_t) as indicated by the proliferation rate. Third, we do not assume that the EGL is an elastic material. Forth, we assume an elastic component radially and circumferentially to the entire cerebellum (k_r), possibly mediated by fibers spanning the cerebellum including those of the Bergmann glia and radial glia as well as the pial surface and meninges covering the cerebellum. And fifth, we posit that the EGL is constrained towards a uniform thickness by fibers spanning the EGL (β), possibly the Bergmann glia. Given the interplay between incompressible material, compressible fibrous material, and a proliferating fluid-like EGL, this model is multiphase.

We constructed an energy functional parameterized by both the inner and outer boundary of the EGL and incorporating the above five assumptions into three dimensionless parameters (μ/k_r, k_r/k_t, k_t/β). We also constrained the parameters with our developmental data. Minimization of the energy functional yields an equation for a driven harmonic oscillator yielding sinusoidal shapes for both the inner and outer boundary of the EGL. In contrast with the elastic bilayer wrinkling model, EGL thickness oscillations are found to be out-of-phase with the surface height (radius) oscillations when $0 < \mu/k_r < 1$. The ratio of these two quantities, the measured surface height amplitude (A_r) and the EGL thickness amplitude (A_t) is given by

$$\frac{A_r}{A_t} = \frac{\frac{\mu}{k_r}}{1 - \frac{\mu}{k_r}} ,$$

which need not be $\gg 1$ as is typical of elastic bilayer wrinkling, and the number of initial folds at E16.5 is determined by

$$n = \sqrt{\frac{k_t}{\beta}} \sqrt{1 + \frac{\frac{\mu}{k_t}}{1 - \frac{\mu}{k_r}}} .$$

Note that in contrast with elastic wrinkling, the number of initial folds does not depend on the thickness (a length scale) of the EGL, but only on material properties.

202 To test the model, we used the observed EGL thickness amplitude, average EGL thickness, average
203 cerebellum radius, and the number of initial folds at E16.5 to constrain 3 of the 5 model parameters. A 4th
204 parameter (u/k_r, denoted as ε) was assumed to scale linearly with time and thus generate predictions of
205 cerebellum shapes at later developmental stages (E17.5 and E18.5). We indeed found that the model well-
206 approximates the phase and amplitude behavior of EGL thickness and radius oscillations, during these
207 stages. (Fig. 5e-g, Supplemental Fig. 6).
208
209 As the model requires radial tension in addition to the circumferential tension demonstrated above, we
210 examined evidence of radial tension between the EGL and the ventricular zone (VZ) at the initiation of
211 folding. Horizontal cuts were made across the core of live E16.5 tissue slices below the EGL and above
212 the VZ that would cut across anterior radial fibers (Fig 5h). As predicted, after cutting, the tissue relaxed
213 revealing tension directed radially within the cerebellum (Fig. 5i,j and Supplemental Fig. 4 and
214 Supplemental Movie 2). Interestingly, quantification of how the radial and horizontal cuts open revealed
215 that only the horizontal cuts opened along the full length of the cut although they opened more slowly
216 than radial cutes (Supplemental Fig. 4g-j), indicating different stress profiles in the two orientations.
217
218 **Hierarchical folding involves differential growth**
219 The cerebellum has hierarchical folding in which the initial folds become subdivided. Given that ACs
220 hold their position during development and compartmentalize granule cells within lobules of the EGL[10]
221 we reasoned that the ACs could be acting as mechanical boundaries enabling similar mechanics to drive
222 the secondary folding. To test this possibility we measured the expansion of the EGL and the core of the
223 individual lobule regions from E18.5 to P3. We found that indeed in the lobule regions that undergo
224 folding there is a temporal correlation between the onset of sub-folding and differential expansion occurs
225 (Fig. 6a-d). In contrast, the region (L45) that does not fold during the same time period has a different,
226 more rectangular shape, and the ratio of EGL growth to core growth is proportional for a rectangle during
227 the time measured (Supplemental Fig. 5). We propose that ACs create mechanical boundaries that divide

228 the cerebellum into fractal-like domains with similar physical properties to the initial unfolded
229 cerebellum. Additionally, since ACs compartmentalize granule cells within the EGL lobule regions[10],
230 once separated the lobule regions can develop distinct characteristics, like the observed differential
231 proliferation rates. We speculate, therefore, that the folding patterns seen across cerebella in different
232 species evolved by adjustment of global as well as regional levels of differential expansion and tension
233 which ultimately mold the functionality of the cerebellum.
234
235 **Discussion**
236 Here we have provided the first evidence that brain folding emerges from a uniform expansion of cells
237 without obvious pre-patterning. Thus, traditional morphometric cellular behaviors such as changes in cell
238 shape, size and proliferation do not direct where cerebellar folding initiates. Furthermore, our
239 developmental interrogation revealed that thickness variations arise in the EGL that are fundamentally
240 inconsistent with traditional elastic bilayer wrinkling models. By applying a novel multiphase model
241 based on the cellular structure of the cerebellum at the time of folding initiation we were able to capture
242 the shape variations with the correct number of folds. The model accounts for: 1) a rapidly expanding
243 fluid-like EGL, whose thickness is regulated by Bergmann glial fibers, 2) a slower growing
244 incompressible core, and 3) fibrous material in the form of glial fibers (and possibly axons) as well as the
245 meninges that provide radial and circumferential tension (Supplemental Fig. 6). One prediction of the
246 model is that adjusting the amount of tension spanning the cerebellum will change the degree of folding.
247 Indeed, alterations of the cells that likely create tension-based forces could explain the dramatically
248 disrupted folding seen in mouse mutants in which radial glia do not produce Bergmann glia[30]. Without
249 Bergmann glia, the EGL would be expected to not form a layer with regular thickness and it should be
250 more sensitive to variations in radial glial tension. Consistent with this prediction, mutants without
251 Bergmann glia have more localized and less regular folds[30]. Our combination of experimental studies and
252 modeling thus provide new insights into brain folding, including an underappreciated role for tension.
253

For our multiphase model to predict the observed shape changes in the murine cerebellum from E17.5 to E18.5 the ratio of the core stiffness over the radial tension must increase. As the measured bulk modulus of the core shows no increase during development, our model predicts that the radial tension must decrease during development. While the cerebellum is crossed by many fibers at folding initiation, radial glial fibers are an attractive candidate to mediate this change in radial tension[31,32]. First, they span from the VZ to the surface of the cerebellum at E16.5. Additionally, during folding initiation the radial glia undergo a transition into Bergmann glia where they release their basal connection to the VZ and the cell body migrates towards the surface[19]. This transition could lead to a reduction in the global radial tension and thus would be consistent with our model prediction.

Finally it is interesting to note the similarities between the developing cerebellum and the cerebral cortex. Radial glia span the entire cerebral cortex just as in the cerebellum[33]. Furthermore, species with folded cerebrums have evolved outer radial glial cells with cell bodies near the surface and fibers that are anchored on the surface, similar to Bergmann glia in the cerebellum[18,34]. Additionally outer radial glial cells proliferate, much like the EGL, to drive the expansion of the outer regions of the cerebral cortex at the time of initiation of folding [35-37]. Moving the zone of proliferation out from the VZ gives more space for the increased proliferation required in folding systems. The cerebellum, housing 80% of the neurons in the human may be an extreme example requiring the region of proliferation to be completely on the outer surface[38]. While we have emphasized the notion of tension via glial fibers in the developing cerebellum, axonal tension has been discussed in the context of shaping the developing cerebrum[39]. Our work calls for a revival of the notion of how tension affects the shape of the developing cerebrum in model mammals like the ferret where experimental testing at the cellular and tissue level are possible. By constraining models with developmental data we will bring about a quantitative understanding of the shaping of the developing brain.

Materials and Methods

Animals.

The inbred FVB/N stain was used for all proliferation rate, area, length, and expansion rate measurements. *Atoh1-CreER*[40], *Nestin-CreER*[41], *Rosa26*^{MTMG,42}, were used to quantify cell shape and size as well as fiber distribution and were maintained on the outbred Swiss Webster background. The Swiss Webster strain was used for scanning acoustic microscopy. Both sexes were used for the analysis. Animals were kept on a 12 hour light/dark cycle and food and water were supplied ad libitum. All experiments were performed following protocols approved by Memorial Sloan Kettering Cancer Center's Institutional Animal Care and Use Committee.

The appearance of a vaginal plug set noon of the day as Embryonic day 0.5 (E0.5). All animals were collected within two hours of noon on the day of collection. Tamoxifen (Tm, Sigma-Aldrich) was dissolved in corn oil (Sigma-Aldrich) at 20 mg/mL. Pregnant females carrying litters with *Atoh1-CreER/+;R26*$^{MTMG/MTMG}$ or *NestinCER/+;R26*$^{MTMG/MTMG}$ embryos were given one 20 µg/g dose of TM via subcutaneous injection two days prior to analysis. 25 µg/g of 5-ethynyl-2-deoxyruidine (EDU; Invitrogen) was administered via subcutaneous injection one hour prior to collection.

Tissue processing, immunohistochemistry, and Imaging

For embryonic stages heads were fixed in 4% paraformaldehyde overnight at 4°C. For postnatal animals, the brain was dissected out first before fixation. Tissues were stored in 30% sucrose. For all proliferation, area, length, and thickness measurements brains were embedded in optimal cutting temperature (OCT) compound. Parasagittal sections were collect with a Leica cryostat (CM3050s) at 10µm.

Prior to IHC, EdU was detected using a commercial kit (Invitrogen, C10340). Following EdU reaction the following primary antibodies were used either overnight at 4°C or 4 hours at room temperature: mouse anti-P27 (BD Pharmingen, 610241), rabbit anti-GFP (Life Technologies, A11122), rat anti-GFP (Nacalai

306 Tesque, 04404-84). All antibodies were diluted to 1:500 in 2% milk (American Bioanalytical) and 0.2%
307 Triton X-100 (Fisher Scientific). Alexa Fluor secondary antibodies (1:500; Invitrogen) were used: Alexa
308 Fluor 488 donkey anti-rabbit, A21206, Alexa Fluor 488 donkey anti-rat, A21208, Alexa Fluor 488
309 donkey anti-mouse, A21202, Alexa Fluor 647 donkey anti-mouse, A31571. EdU was detected using a
310 commercial kit (Invitrogen, C10340).
311
312 For cell size, shape and fiber density analysis 60 µm parasagittal sections were collected on a Leica
313 vibratome (VT100S). Primary and secondary antibodies were diluted 1:500 in 2% milk and incubated
314 overnight at 4°C.
315
316 For scanning acoustic microscopy brains were processed for paraffin embedding and parasagittal sections
317 of 10 µm thick were collected on a microtome (Leica RM2255). Structured illumination and confocal
318 Imaging was done with Zeiss Observer Z.1 with Apatome or Zeiss LSM 880 respectively.
319
320 **Quantification of Proliferation, Length, Area, Folding Index and Thickness**
321 Measurements for all analysis were taken from the three most midline sagittal sections and averaged. The
322 most midline section was determined by dividing the distance in half between the lateral edges where the
323 third ventrical and the mesencephalic vesicle are no longer connected. Quantifications were made using
324 Imaris (Bitplane) and Matlab (Mathworks) software.
325
326 EGL Proliferation rate was calculated as EDU+/(Dapi+;P27-) cells. All cells were counted within the
327 lobule region to the midpoint of the Anchoring Centers. For proliferation measurements through the ACs
328 and the surrounding EGL at E16.5 and E17.5 a 50 µm window measured from the outer surface of the
329 EGL was centered at the AC. The measuring window was centered at every 25 µm anterior and posterior
330 to the EGL for a total distance of 250 µM anterior and posterior to the AC. At E18.5, when the AC is fully
331 formed, everything proximal to the centroid of the cerebellum under the midpoint of the AC was counted

332 as the AC. Non-overlapping regions of 50 μm also were measured in either direction for a total of 200 μM
333 anterior and posterior to the AC. Proliferation was measured in 3 cerebella at E16.5 and E17.5 and in 4
334 cerebella at E18.5
335
336 EGL length was measured from the outer surface of the EGL following the curvature of the EGL.
337 Cerebellar area was calculated as the area within the outer surface of the EGL and the ventricular zone. A
338 short strait edge was made perpendicular to the ventricular zone to close the area back upon to the anterior
339 end of the EGL. The convex curvature of the cerebellum was measured by following only the positive
340 curvature of the EGL. The folding index was determined as FI = 1 - (Positive curvature/EGL length).
341 Data collected for E16.5, E17.5, E18.5 and P0 came from 6,8,7, and 9 cerebella respectively.
342 EGL thickness was measured by defining the outer and inner curvature of the EGL. The shortest distance
343 lines were drawn to the outer curvature from discrete points distributed at every 12.5 μm along the inner
344 curvature of the EGL. Nine ACs and surrounding regions from five cerebella were quantified at E16.5 and
345 13 ACs from five cerebellar were analyzed at E17.5. At E18.5 six ACs from two cerebellar were
346 quantified.
347
348 **Quantification of Cell Shape**
349 Midline sections were imaged with a Zeiss LSM 880. Serial images were taken to cover the entire EGL of
350 lobule regions L123, L45, and L678 and the ACs. Manual cell masks were created with Imaris software
351 defining the curvature at every z-slice. Every cell that was completely included in the imaging window
352 and that was distinguishable from surrounding cells was counted to reduce sampling bias. Cells from
353 three brains were measured at each stage for a total of 131 at E16.5 and 201 at E18.5. Shape was defined
354 via sphericity, which is the surface area of a sphere having the same volume as the cell of interest divided
355 by the surface area of the cell of interest.
356
357 **Quantification of Fibers within the EGL**

358 Midline sections were imaged with a Zeiss LSM 880. Image tiling was used to cover the EGL. Using
359 Python, a 4th or 5th order polynomial was fitted to the outer edge of the EGL in each image, and five scan
360 lines were positioned at 12.2 μm intervals beneath the surface, and parallel to it. A bin width of 50 μm as
361 measured along the polynomial contour was centered at the AC. Bins of equal distance were extended
362 both anteriorly and posteriorly. Staining intensity was counted along each scan line at every z-slice of the
363 confocal stack. Each image was normalized to the mean intensity and smoothed with a Gaussian filter.
364 Peak counting was done using minimum and maximum filters, keeping neighborhood size and threshold
365 parameters constant for all datasets. The results from the 5 scan lines were averaged.
366
367 **Tissue cutting**
368 Live cerebella of E16.5 FVB/N mice were collected in dissection buffer as previously described[43] and
369 embedded in low-melting point agarose (Invitrogen). Sagittal slices at a thickness of 250 microns were
370 collected. Slices were removed from the agarose and place in petri-dishes coated with Poly(2-
371 hydroxyethyl methacrylate)(Sigma-Aldrich). Tissue cuts were made with a 30° Premier Edge stab knife
372 (Oasis Medical). Slices were allowed to relax for 10 minutes. Time-lapse images were acquired on a
373 Leica MZ75 dissection scope.
374
375 **Scanning Acoustic Microscopy**
376 Mechanical tissue properties were analyzed using a 250 MHz Scanning Acoustic Microscope (SAM),
377 described previously[44,45]. Briefly, 12 μm paraffin sections of mouse embryonic brains were de-
378 parafinized, hydrated in de-ionized water and scanned on the SAM to generate maps of amplitude, sample
379 thickness, speed of sound, acoustic impedance, attenuation, bulk modulus, and mass density. Co-
380 registered histology and SAM amplitude images were used to identify regions-of-interest (ROIs)
381 corresponding to the EGL layer and underlying core of the cerebellum in each sample. Bulk modulus was
382 analyzed as a measure of tissue stiffness: ROI measurements were acquired from 3 sections from 3
383 embryos at each developmental stage.

Finite element simulations

The wrinkle of a circular bilayer structure in Fig. 3a was simulated with commercial software ABAQUS. Both film and substrate were modeled as incompressible neo-Hookean materials. The ratio between shear moduli of the film and substrate was 50 and the initial radius of the simulated structure was 16 times that of the film thickness. The differential growth of the EGL and core was modeled by an isotropic expansion of the film in the bilayer structure.

To test the elastic wrinkling model, we conducted finite element (FE) simulations for bilayer structures with a film bonded on a substrate, which represents the EGL layer and core structure, respectively. The structures were assumed to be under 2D plane strain deformation to mimic the quasi-2D nature of cerebellum wrinkles. Neo-Hookean model was adopted to describe the elastic properties of both film and substrate, whose strain energy can be expressed as

$$U = \frac{1}{2}\mu(I_1 - 3)$$

where μ is the shear modulus and I_1 represents the first invariant of the deformation gradient tensor $\boldsymbol{F}$. The Poisson's ratios for the film and substrate were set to be 0.5, based on experimental observations that the bulk modulus of EGL and core are in the order of GPa, much larger than the shear modulus of soft tissues (~ kPa).

We carried out FE simulations through commercial software ABAQUS. A second order 6 node hybrid element (CPE6MH) was utilized to discretize the film and substrate. Very fine FE meshes were used to make sure the results independent of mesh size. To incorporate differential growth in real EGL layer and core, an isotropic growth deformation tension was applied to the modeled film by decoupling the deformation tenor $\boldsymbol{F}$ into elastic deformation part $\boldsymbol{A}$ and growth part $\boldsymbol{G}$.

$$\boldsymbol{F} = \boldsymbol{A} \cdot \boldsymbol{G}$$

For simplicity, we assume the growth part is isotropic and controlled by a scalar variable g

$$\boldsymbol{G} = g\begin{bmatrix}1 & 0 & 0\\0 & 1 & 0\\0 & 0 & 1\end{bmatrix}$$

where $g > 1$ represents a faster growth in EGL than the core. To trigger instabilities in numerical simulations, random perturbations (e.g., White Gaussian noise with $0.001t$ mean magnitude) were applied to the nodal positions at the top surface of the film and the interface between the film and substrate.

To qualitatively understand the cut experiments we ran a FE simulation of a pre-cut circular bilayer structure and then assigned swelling strain to the film. This neglected the dynamical process in the real cut experiments and only focused on the final equilibrium of the cerebellum after long time relaxation. All the simulation parameters were the same as those in the wrinkling simulation. The initial cut length a is equal to $8t$. The minimum in-plane principal stress corresponds to the hoop stress in the film.

Methods for modeling initiation of cerebellar folds

We considered the midsagittal section of the cerebellum and, therefore, formulated a two-dimensional model. The distance of the outer edge of the EGL and, hence, the outer edge of the cerebellum from the center of the cerebellum was defined as r(θ) with θ as the angular coordinate. We assumed that r(θ) was single-valued. The thickness of the EGL was defined as t(θ). See model schematic below.

Taking into account the four assumptions discussed in the main text, we constructed the following energy functional to be minimized

$$E\left[r, t, \frac{dt}{d\theta}\right] = \int d\theta\, \{k_r(r - r_0)^2 - k_t(t - t_0)^2 + \beta\, \left(\frac{dt}{d\theta}\right)^2\},$$

with k_r as the stiffness modulus (a spring constant in one-dimension) of the radial glial fibers and the pial surface contained in the meninges surrounding the cerebellum since the cerebellar radius is proportional

to its perimeter, r_0 as the preferred radius of the cerebellum, k_t denoting a growth potential due to cell proliferation, t_0 as thickness of the EGL (cortex), and, β quantified the mechanical resistance to changing the thickness of the EGL. Given our first assumption of an incompressible cerebellar core, we imposed the constraint

$$\frac{1}{2}\int d\theta\,(r-t)^2 = A_0,$$

with A_0 as a preferred cerebellar area. We applied the variational principle to minimize the energy functional subject to the core constraint, i.e.

$$\delta(E - \mu\int d\theta\,(r-t)^2) = 0,$$

where μ is a Lagrange multiplier. Assuming the preferred radius of the cerebellum is constant and the thickness of the EGL/cortex is also constant, then the preferred cerebellar shape was a circle and the EGL an annulus.

The variational analysis yielded the following equation of shape for t(θ);

$$\frac{d^2t}{d\theta^2} + q^2\,t(\theta) = \frac{k_t}{\beta}\left(t_0 + \frac{\frac{\mu r_0}{k_t}}{1-\frac{\mu}{k_r}}\right),$$

with $q^2 = \frac{k_t}{\beta}\left(1 + \frac{\frac{\mu}{k_t}}{1-\frac{\mu}{k_r}}\right)$. The solution to the equation of shape was

$$t(\theta) = A_t\sin(q\theta + \phi) + C_1(r_0, t_0, k_r, k_t, \mu),$$

with C_1 independent of θ and $A_t = \sqrt{2}\left(1-\frac{\mu}{k_r}\right)\sqrt{\frac{A_0}{\pi} - C_2(r_0, t_0, k_r, k_t, \mu)}$ such that $A_0 > \pi C_2$. There was an additional equation of shape for r(θ) from the variational principle that depended on t(θ) and so was determined

$$r(\theta) = -\frac{\frac{\mu}{k_r}}{1-\frac{\mu}{k_r}} A_t \sin(q\theta + \phi) + C_3(r_0, k_r, \mu).$$

We used the measured data at E16.5 to set the parameters to make predictions for the shape of both the EGL and core (and so the relationship between the two) at later times. Plots assumed a circular preferred shape, and with other parameters as follows: $\epsilon = \mu/k_r$ is shown in Fig. 5f, $c = k_r/k_t = 0.06/\epsilon$, $A_t/r_0 = \epsilon/9.6$, $t_0/r_0 = \epsilon/4.8$, and $q = 6$. Note that for $\epsilon = 0.3$, these parameters are numerically consistent with our E16.5 measurements: $A_t/t_0 = 0.5$ and $r_0/t_0 = 16$, as well as the observed number of invaginations in the half circle: $q/2 = 3$. All of these parameters are either constant or depend on the time-like parameter ϵ. One of these dependencies has a functional form that is physically justifiable ($A_t \sim \epsilon$), another has a form that is biologically justifiable ($c \sim 1/\epsilon$), owing to the decrease in the number of radial glia over time.

We defined a dimensionless "shape factor" as half of the perimeter divided by the square root of half of the area as appropriate for a semi-circle. To compare the model's predictive deviation of this quantity form the semi-circular value we assumed a linear relationship between ϵ and time t measured in embryonic days: $\epsilon(t) = 0.3(t-15.5)$.

Statistical analyses

Statistical analyses were performed using Matlab software. Significance was determined at $P < 0.05$. Two-way ANOVA was used for proliferation analysis as two variables were tracked, mouse and region. Cell shape, volume, fiber distribution, EGL thickness and bulk modulus were run under a standard ANOVA. After ANOVA analysis a multiple comparison was run with Tukey's honestly significant difference

criterion. F-test for variance and two-tailed student's paired t-test were used for slice cutting and relaxation quantifications. The degrees of freedom, test statistics, and P values, are given in the figure legends, where appropriate. All error bars are standard deviations. No statistical methods were used to predetermine the sample sizes. We used sample sizes aligned with the standard in the field. No randomization was used nor was data collection or analysis performed blind.

Acknowledgements We are grateful to Anna-Katerina Hadjantonakis and Songhai Shi for use of Imaris software. We thank Jennifer Zallen and Anna-Katerina Hadjantonakis for experimental advice, Nathanael Kim for help with the acoustic microscopy and Professor Tadashi Yamagushi for his support for MO's visit to New York. We appreciate the discussions we have had with Alexandre Wojcinski and the entire Joyner Laboratory, and the administrative support from Cara Monaco. This work was supported by grants from the NIH to ALJ (R37MH085726 and R01NS092096) and A.K.L (F32 NS086163) and a National Cancer Institute Cancer Center Support Grant (P30 CA008748-48). T.A.E. and J.M.S. acknowledge financial support from NSF-DMR-CMMT Award Number 1507938 and NSF-PHY-PoLS Award Number 1607416. FE simulations were performed at the Comet cluster (Award no. TG-MSS170004) in XSEDE. The development of the acoustic microscopy instrument and signal-processing methods was supported by NIH grant R21EB016117 awarded to J.M.

Author Contributions

A.K.L. and A.L.J. conceived the project; T.E., T.Z. and J.M.S. designed and performed the modeling, A.K.L and A.L.J. designed the experimental research; A.K.L performed the experiments; D.R., M.O., J.M. and D.T. performed the acoustic microcopy experiments and analyzed the data; all authors discussed the data; A.K.L. and A.L.J. wrote the manuscript with contributions from all authors.

Competing Interests The authors declare no competing interests.

Correspondence and requests for materials should be addressed to A.L.J.

References

1 Tallinen, T., Chung, J. Y., Biggins, J. S. & Mahadevan, L. Gyrification from constrained cortical expansion. *Proceedings of the National Academy of Sciences of the United States of America* **111**, 12667-12672, doi:10.1073/pnas.1406015111 (2014).

2 Ronan, L. *et al.* Differential tangential expansion as a mechanism for cortical gyrification. *Cerebral cortex* **24**, 2219-2228, doi:10.1093/cercor/bht082 (2014).

3 Bayly, P. V., Okamoto, R. J., Xu, G., Shi, Y. & Taber, L. A. A cortical folding model incorporating stress-dependent growth explains gyral wavelengths and stress patterns in the developing brain. *Physical biology* **10**, 016005, doi:10.1088/1478-3975/10/1/016005 (2013).

4 Xu, G. *et al.* Axons pull on the brain, but tension does not drive cortical folding. *J Biomech Eng* **132**, 071013, doi:10.1115/1.4001683 (2010).

5 Hohlfeld, E. & Mahadevan, L. Unfolding the sulcus. *Physical review letters* **106**, 105702, doi:10.1103/PhysRevLett.106.105702 (2011).

6 Bayly, P. V., Taber, L. A. & Kroenke, C. D. Mechanical forces in cerebral cortical folding: a review of measurements and models. *Journal of the mechanical behavior of biomedical materials* **29**, 568-581, doi:10.1016/j.jmbbm.2013.02.018 (2014).

7 Lejeune, E., Javili, A., Weickenmeier, J., Kuhl, E. & Linder, C. Tri-layer wrinkling as a mechanism for anchoring center initiation in the developing cerebellum. *Soft matter* **12**, 5613-5620, doi:10.1039/c6sm00526h (2016).

8 Tallinen, T. *et al.* On the growth and form of cortical convolutions. *Nature Physics* **12**, 588-593, doi:10.1038/nphys3632 (2016).

9 Leto, K. *et al.* Consensus Paper: Cerebellar Development. *Cerebellum* **15**, 789-828, doi:10.1007/s12311-015-0724-2 (2016).

10 Legue, E., Riedel, E. & Joyner, A. L. Clonal analysis reveals granule cell behaviors and compartmentalization that determine the folded morphology of the cerebellum. *Development* **142**, 1661-1671, doi:10.1242/dev.120287 (2015).

11 Legue, E. *et al.* Differential timing of granule cell production during cerebellum development underlies generation of the foliation pattern. *Neural development* **11**, 17, doi:10.1186/s13064-016-0072-z (2016).

12 Sudarov, A. & Joyner, A. L. Cerebellum morphogenesis: the foliation pattern is orchestrated by multi-cellular anchoring centers. *Neural development* **2**, 26, doi:10.1186/1749-8104-2-26 (2007).

13 T. A. Engstrom, T. Z., A.K. Lawton, A.L. Joyner, and J.M. Schwarz. Buckling without bending: A new paradigm in morphogenesis. *arXiv* **1806.06961** (2018).

14 Mammoto, T. & Ingber, D. E. Mechanical control of tissue and organ development. *Development* **137**, 1407-1420, doi:10.1242/dev.024166 (2010).

15 Harding, M. J., McGraw, H. F. & Nechiporuk, A. The roles and regulation of multicellular rosette structures during morphogenesis. *Development* **141**, 2549-2558, doi:10.1242/dev.101444 (2014).

16 Stemple, D. L. Structure and function of the notochord: an essential organ for chordate development. *Development* **132**, 2503-2512, doi:10.1242/dev.01812 (2005).

17 He, B., Doubrovinski, K., Polyakov, O. & Wieschaus, E. Apical constriction drives tissue-scale hydrodynamic flow to mediate cell elongation. *Nature* **508**, 392-396, doi:10.1038/nature13070 (2014).

18 Leung, A. W. & Li, J. Y. H. The Molecular Pathway Regulating Bergmann Glia and Folia Generation in the Cerebellum. *Cerebellum* **17**, 42-48, doi:10.1007/s12311-017-0904-3 (2018).

19 Yuasa, S. Bergmann glial development in the mouse cerebellum as revealed by tenascin expression. *Anat Embryol (Berl)* **194**, 223-234 (1996).

20 Yamada, K. & Watanabe, M. Cytodifferentiation of Bergmann glia and its relationship with Purkinje cells. *Anat Sci Int* **77**, 94-108, doi:10.1046/j.0022-7722.2002.00021.x (2002).

21 Richman, D. P., Stewart, R. M., Hutchinson, J. W. & Caviness, V. S., Jr. Mechanical model of brain convolutional development. *Science* **189**, 18-21 (1975).

22 Nelson, C. M. On Buckling Morphogenesis. *J Biomech Eng* **138**, 021005, doi:10.1115/1.4032128 (2016).
23 Hannezo, E., Prost, J. & Joanny, J.-F. *Mechanical Instabilities of Biological Tubes*. Vol. 109 (2012).
24 Shyer, A. E. *et al.* Villification: How the Gut Gets Its Villi. *Science (New York, N.Y.)* **342**, 212-218, doi:10.1126/science.1238842 (2013).
25 Wiggs, B. R., Hrousis, C. A., Drazen, J. M. & Kamm, R. D. On the mechanism of mucosal folding in normal and asthmatic airways. *J Appl Physiol (1985)* **83**, 1814-1821, doi:10.1152/jappl.1997.83.6.1814 (1997).
26 Mota, B. & Herculano-Houzel, S. BRAIN STRUCTURE. Cortical folding scales universally with surface area and thickness, not number of neurons. *Science* **349**, 74-77, doi:10.1126/science.aaa9101 (2015).
27 Allen, H. G. *Analysis and design of structural sandwich panels*. 1st edn, (Pergamon Press, 1969).
28 Zhao, R. & Zhao, X. *Multimodal Surface Instabilities in Curved Film-Substrate Structures*. Vol. 84 (2017).
29 Budday, S. *et al.* Rheological characterization of human brain tissue. *Acta Biomater* **60**, 315-329, doi:10.1016/j.actbio.2017.06.024 (2017).
30 Li, K., Leung, A. W., Guo, Q., Yang, W. & Li, J. Y. Shp2-dependent ERK signaling is essential for induction of Bergmann glia and foliation of the cerebellum. *The Journal of neuroscience : the official journal of the Society for Neuroscience* **34**, 922-931, doi:10.1523/JNEUROSCI.3476-13.2014 (2014).
31 Sillitoe, R. V. & Joyner, A. L. Morphology, molecular codes, and circuitry produce the three-dimensional complexity of the cerebellum. *Annu Rev Cell Dev Biol* **23**, 549-577, doi:10.1146/annurev.cellbio.23.090506.123237 (2007).
32 Rahimi-Balaei, M. *et al.* Embryonic stages in cerebellar afferent development. *Cerebellum Ataxias* **2**, 7, doi:10.1186/s40673-015-0026-y (2015).
33 Gotz, M., Hartfuss, E. & Malatesta, P. Radial glial cells as neuronal precursors: a new perspective on the correlation of morphology and lineage restriction in the developing cerebral cortex of mice. *Brain Res Bull* **57**, 777-788 (2002).
34 Reillo, I., de Juan Romero, C., Garcia-Cabezas, M. A. & Borrell, V. A role for intermediate radial glia in the tangential expansion of the mammalian cerebral cortex. *Cerebral cortex* **21**, 1674-1694, doi:10.1093/cercor/bhq238 (2011).
35 Hansen, D. V., Lui, J. H., Parker, P. R. & Kriegstein, A. R. Neurogenic radial glia in the outer subventricular zone of human neocortex. *Nature* **464**, 554-561, doi:10.1038/nature08845 (2010).
36 Heng, X., Guo, Q., Leung, A. W. & Li, J. Y. Analogous mechanism regulating formation of neocortical basal radial glia and cerebellar Bergmann glia. *eLife* **6**, doi:10.7554/eLife.23253 (2017).
37 Nowakowski, T. J., Pollen, A. A., Sandoval-Espinosa, C. & Kriegstein, A. R. Transformation of the Radial Glia Scaffold Demarcates Two Stages of Human Cerebral Cortex Development. *Neuron* **91**, 1219-1227, doi:10.1016/j.neuron.2016.09.005 (2016).
38 Andersen, B. B., Korbo, L. & Pakkenberg, B. A quantitative study of the human cerebellum with unbiased stereological techniques. *J Comp Neurol* **326**, 549-560, doi:10.1002/cne.903260405 (1992).
39 Van Essen, D. C. A tension-based theory of morphogenesis and compact wiring in the central nervous system. *Nature* **385**, 313-318, doi:10.1038/385313a0 (1997).
40 Machold, R. & Fishell, G. Math1 is expressed in temporally discrete pools of cerebellar rhombic-lip neural progenitors. *Neuron* **48**, 17-24, doi:10.1016/j.neuron.2005.08.028 (2005).
41 Isaka, F. *et al.* Ectopic expression of the bHLH gene Math1 disturbs neural development. *The European journal of neuroscience* **11**, 2582-2588 (1999).
42 Muzumdar, M. D., Tasic, B., Miyamichi, K., Li, L. & Luo, L. A global double-fluorescent Cre reporter mouse. *Genesis* **45**, 593-605, doi:10.1002/dvg.20335 (2007).

601 43 Wojcinski, A. *et al.* Cerebellar granule cell replenishment postinjury by adaptive reprogramming
602 of Nestin(+) progenitors. *Nature neuroscience* **20**, 1361-1370, doi:10.1038/nn.4621 (2017).
603 44 Rohrbach, D., Lloyd, H. O., Silverman, R. H. & Mamou, J. Fine-resolution maps of acoustic
604 properties at 250 MHz of unstained fixed murine retinal layers. *The Journal of the Acoustical*
605 *Society of America* **137**, EL381-387, doi:10.1121/1.4916790 (2015).
606 45 Rohrbach, D. *et al.* Improved High-Frequency Ultrasound Corneal Biometric Accuracy by
607 Micrometer-Resolution Acoustic-Property Maps of the Cornea. *Translational vision science &*
608 *technology* **7**, 21, doi:10.1167/tvst.7.2.21 (2018).

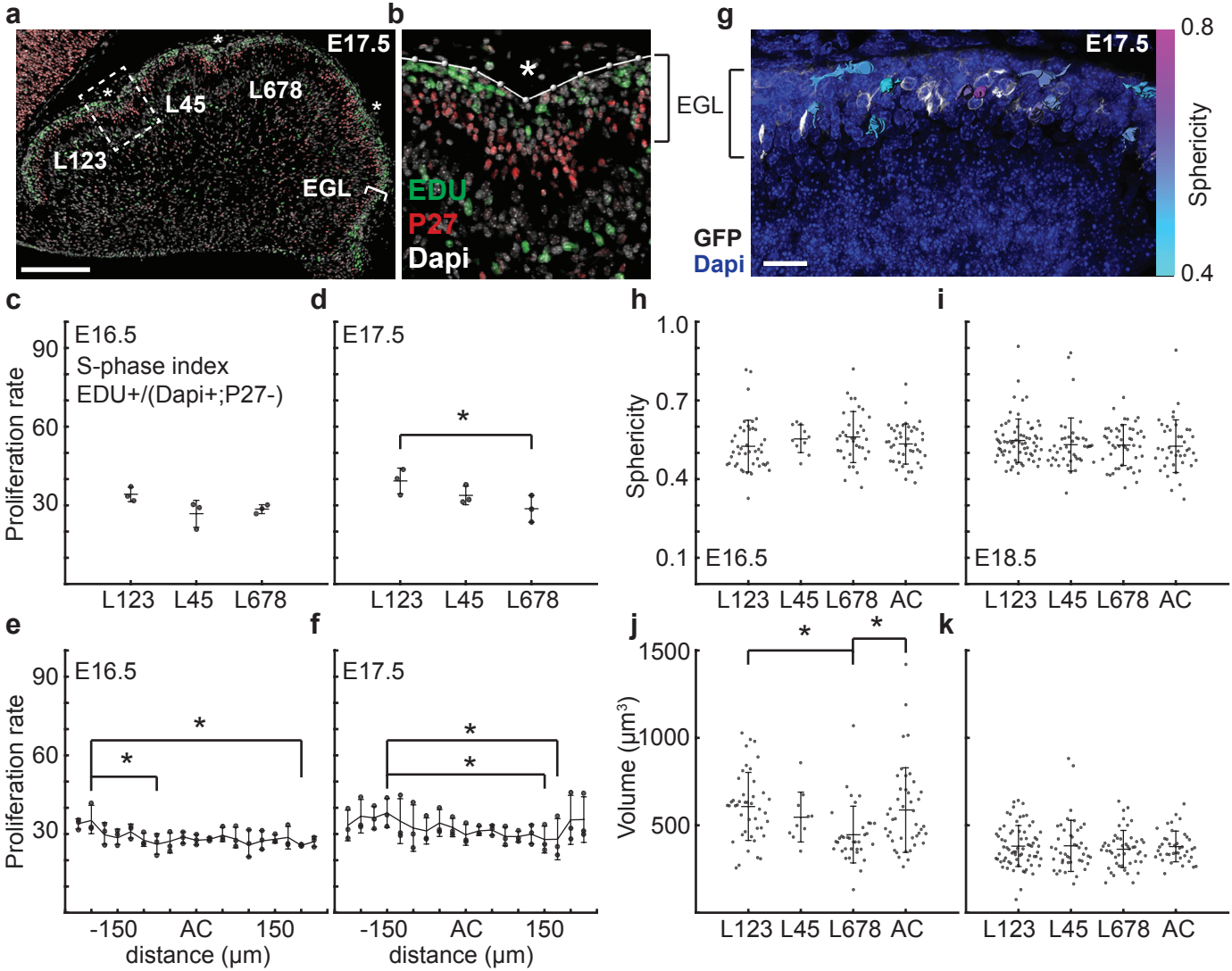

Fig. 1: At folding initiation the EGL has uniform proliferation, cell size, and cell shape. a,b Low and high power images of immuno-histochemical (IHC) staining of sagittal cerebellar sections to measure proliferation in the lobule (L) indicated at 25 µm windows surrounding the ACs (stars). Scale bar: 200 µm. **c,d**, EGL Proliferation is uniform before and during the onset of invagination (Two-way anova: df = 2. **c** P = 0.10, F = 4.36 **d** P = 0.03, F = 10.31). **e,f**, Proliferation in the AC is uniform with the surrounding EGL (Two-way anova: df = 18. **e** P = 0.03, F = 2.15 **f** P =2.1e^{-3} F = 3.06). **g**, Section of Atoh1-CreER/+; R26MTMG/+ E16.5 cerebellum showing masked labeled cells. Scale bar: 20 µm. **h,i**, Cell shape is uniform before and during folding (anova df = 3. **h** P = 0.34, F = 1.13 **i** P = 0.61,F = 0.61). **j,k**, Cell size is uniform (anova df = 3. **j** P =3.6e^{-3} F = 4.75 , **k** P = 0.85, F = 0.26). Stars indicate statistical differences. Error bars: S.D.

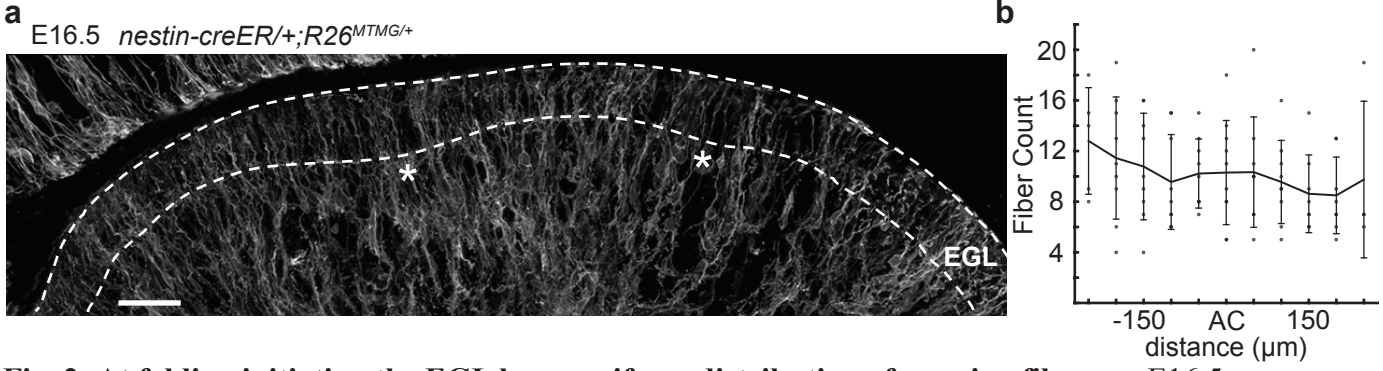

Fig. 2: At folding initiation the EGL has a uniform distribution of crossing fibers. a, E16.5 *nestin-CreER/+; R26$^{MTMG/+}$* cerebellum section showing IHV labeling of radial and Bergmann glial fibers. Stars: AC. Dotted lines denote EGL. Scale bar: 50 µm. b, Fiber density in the ACs is uniform with the surrounding EGL (anova df = 10; P = 0.76, F = 0.66). Error bars: S.D.

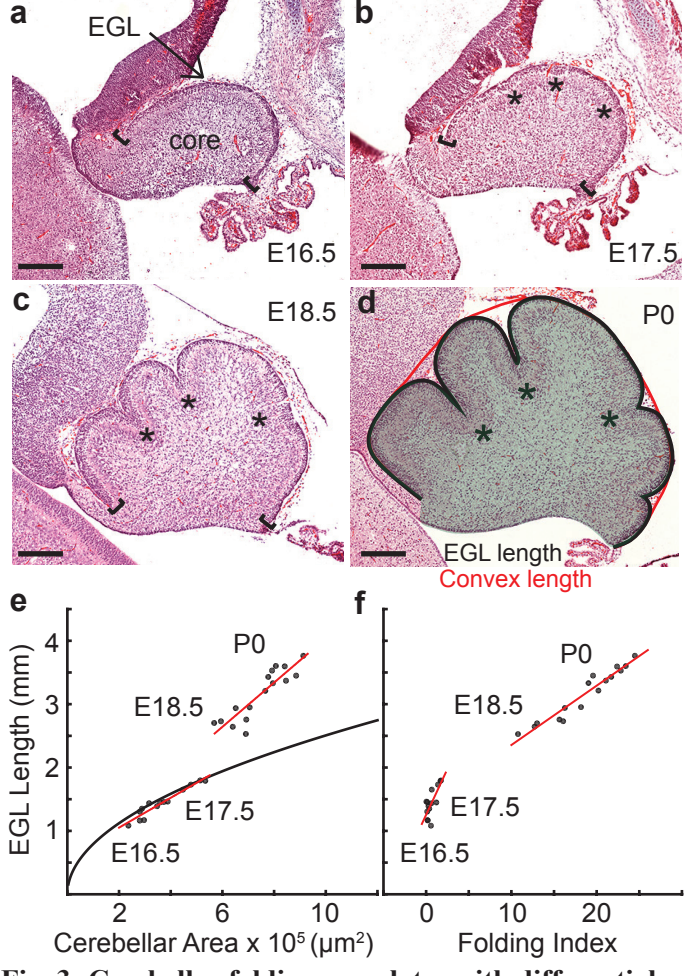

Fig. 3: Cerebellar folding correlates with differential expansion. a-d, H&E stained midline sagittal sections of FVB/N mice. Stars: ACs. Brackets: anterior/posterior ends of the EGL. Black line and red line in (**d**): EGL and convex length, respectively. Shaded area: core. **e**, At E16.5 and E17.5 expansion of EGL length and cerebellar area fit the proportional expansion of a semi-circle (curve). At E18.5 and P0 EGL expansion is greater than core area growth creating differential expansion. **f**, Folding index [1 - (convex length/EGL length) x 100] reveals folding initiates during differential expansion. Scale bars: 200 μm.

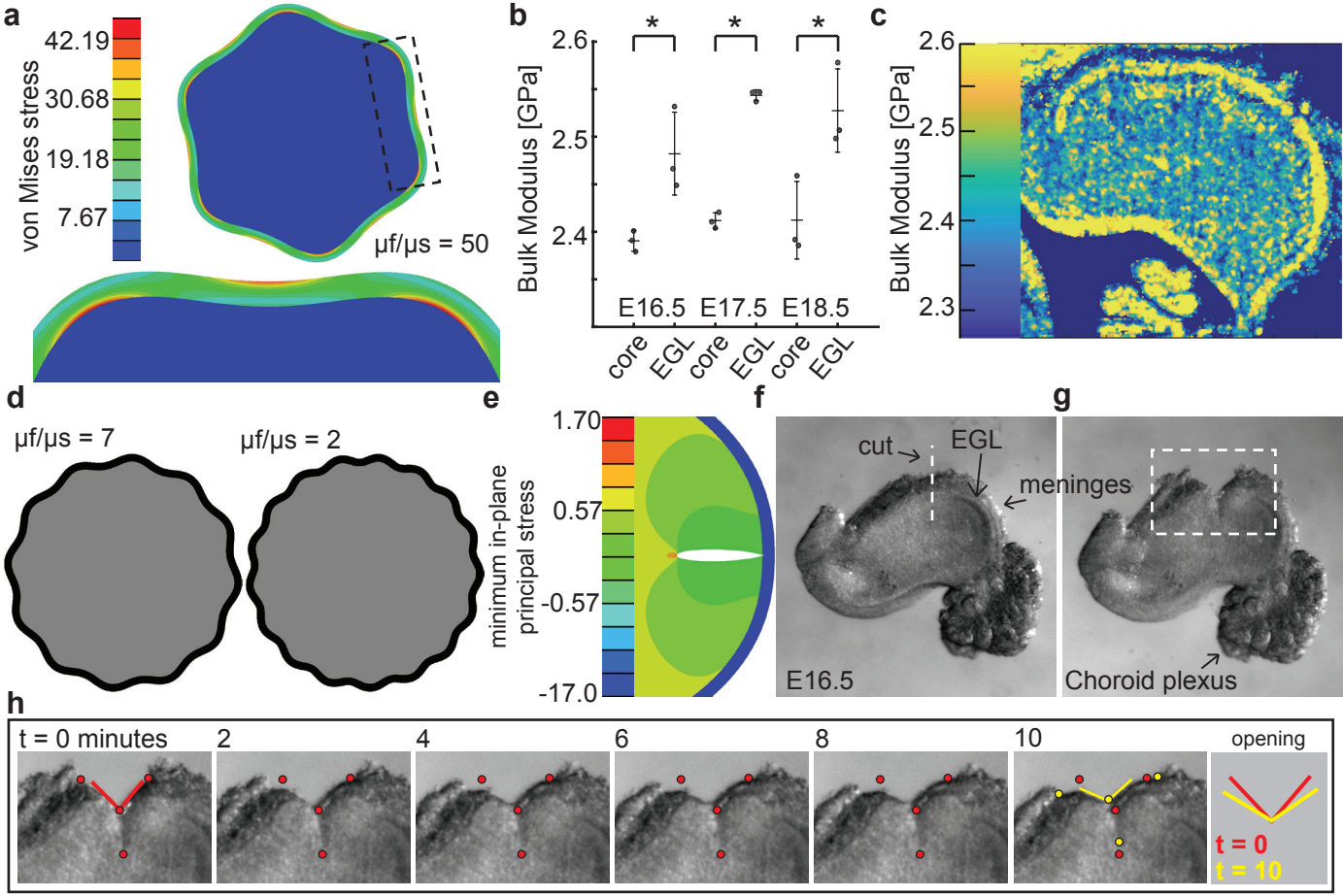

Fig. 4: Measured tissue stiffness and stress at folding initiation are inconsistent with wrinkling models. a, Inducing the correct number of folds through a wrinkling model require a stiffness differential between the layers of 50 fold (μf/μs = 50, g = 1.05). **b,c**, Acoustic mapping of cerebellar slices show a stiffer EGL than core at each stage (anova df = 5; P = 1.0e^{-4} F = 13.59), but not the required differential. Stars indicate statistical differences. Error bars: S.D. **d**, Wrinkling simulations constrained by developmental data produce wavelengths inconsistent with the cerebellum. **e**, Simulations predict the EGL remains closed after cutting. **f,g**, Images of a live cerebellar slice before and after cutting, and images from time lapse movie, **h**, show the EGL opens, revealing circumferential tension along the EGL. Red and yellow dots: cut edges. Lines: relaxation angle.

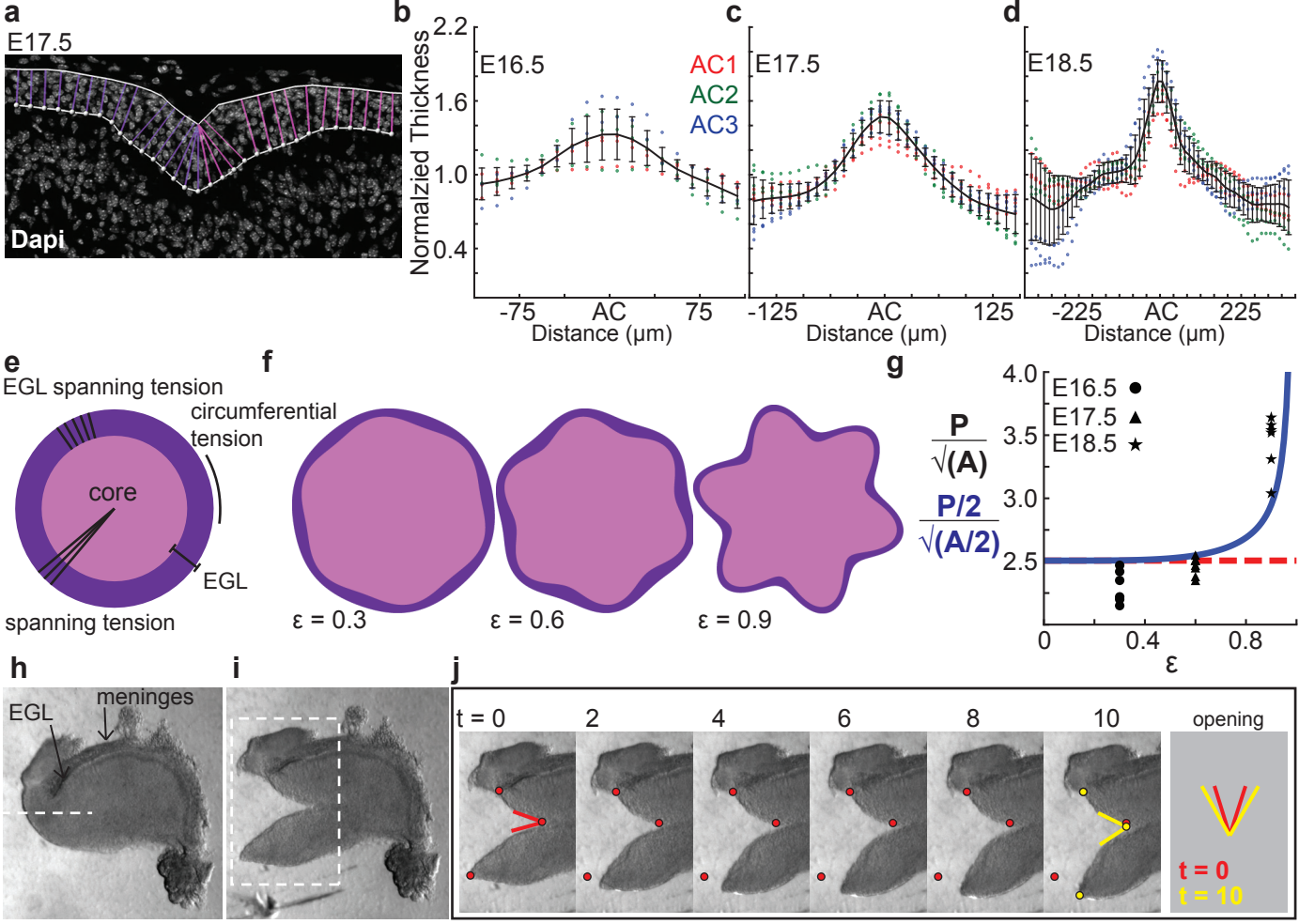

Fig. 5: A multiphase model with radial and circumferential constraints and liquid-fibrous EGL composition approximates cerebellar folding. a, Staining of nuclei with EGL outlined and lines used to measure thickness. **b-d**, EGL thickness at the ACs increases during folding initiation (anova E16.5 df = 29, P = $8.2e^{-20}$ F = 12.59. E17.5 df = 29, P = $3.4e^{-116}$ F = 62.78, E18.5 df = 57, P = $6.8e^{-67}$ F = 13.28). At E16.5 only brains with visible ACs were included. Error bars: S.D. **e**, Schematic of multiphase model showing types of tension. **f**, Thickness variations arise concomitant with folding. **g** Shape factor analysis: semicircle (red), model shape prediction (blue) measured shape (black). Assumed linear relationship between ε and time, ε(t) = 0.3(t -15.5). **h-j** Tissue cutting reveals radial tension between the EGL and the VZ. Red and yellow dots: cut edges at t = 0 and t = 10. Lines: relaxation angle.

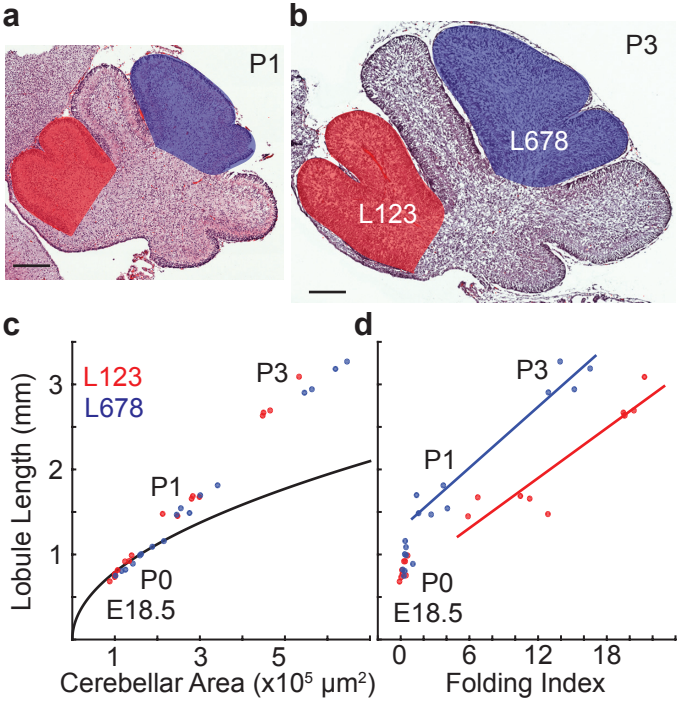

Fig. 6: Progressive folding occurs during regional differential expansion. a,b, H&E stained midline sagittal sections of FVB/N cerebella at P1 and P3. **c**, Expansion of lobule length and lobule area approximate the proportional expansion of a semi-circle (curve) at E18.5 and P0. After P0 the EGL expansion in both regions increases more than the underlying area creating differential expansion. **d**, Folding initiates during regional differential expansion. Scale bars: 200 μm.

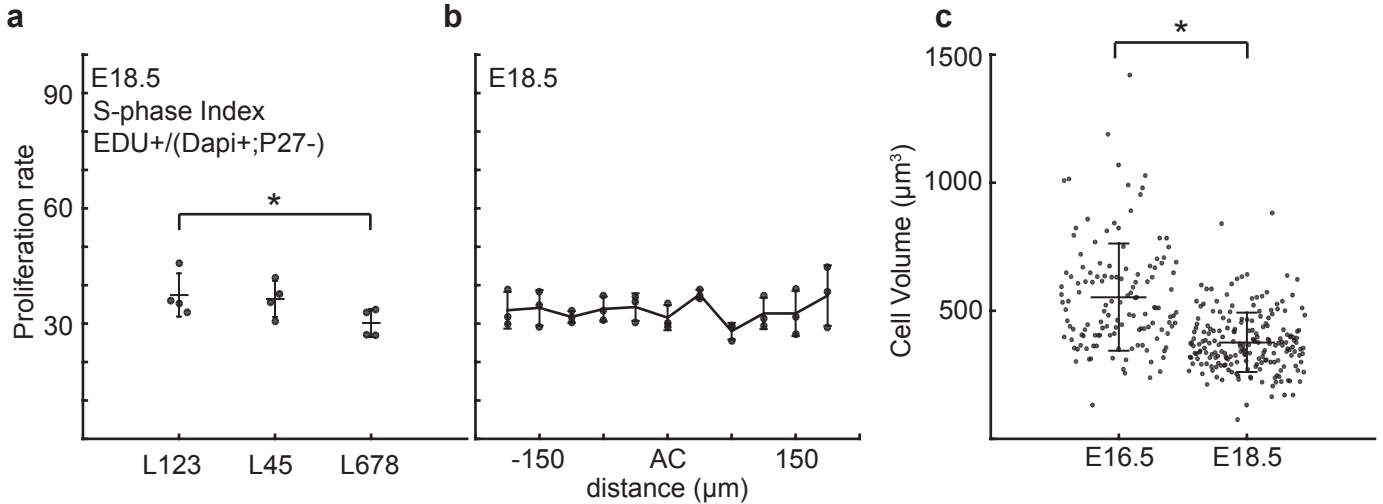

Supplemental Fig. 1: Proliferation rate is reduced in the central zone of the cerebellum after folding initiation. a, Proliferation is reduced in lobule region L678 compared to other lobules (anova: df = 2; P = 0.01, F = 9.24). **b**, Proliferation through the AC regions is uniform with the surrounding EGL (anova: df = 10; P = 0.17, F = 1.64). **c**, At E18.5 cells within the EGL are smaller than at earlier stages (two-tailed t-test df = 330 P = $2.92e^{-20}$, T = 9.85). Stars: statistical differences. Error bars: S.D.

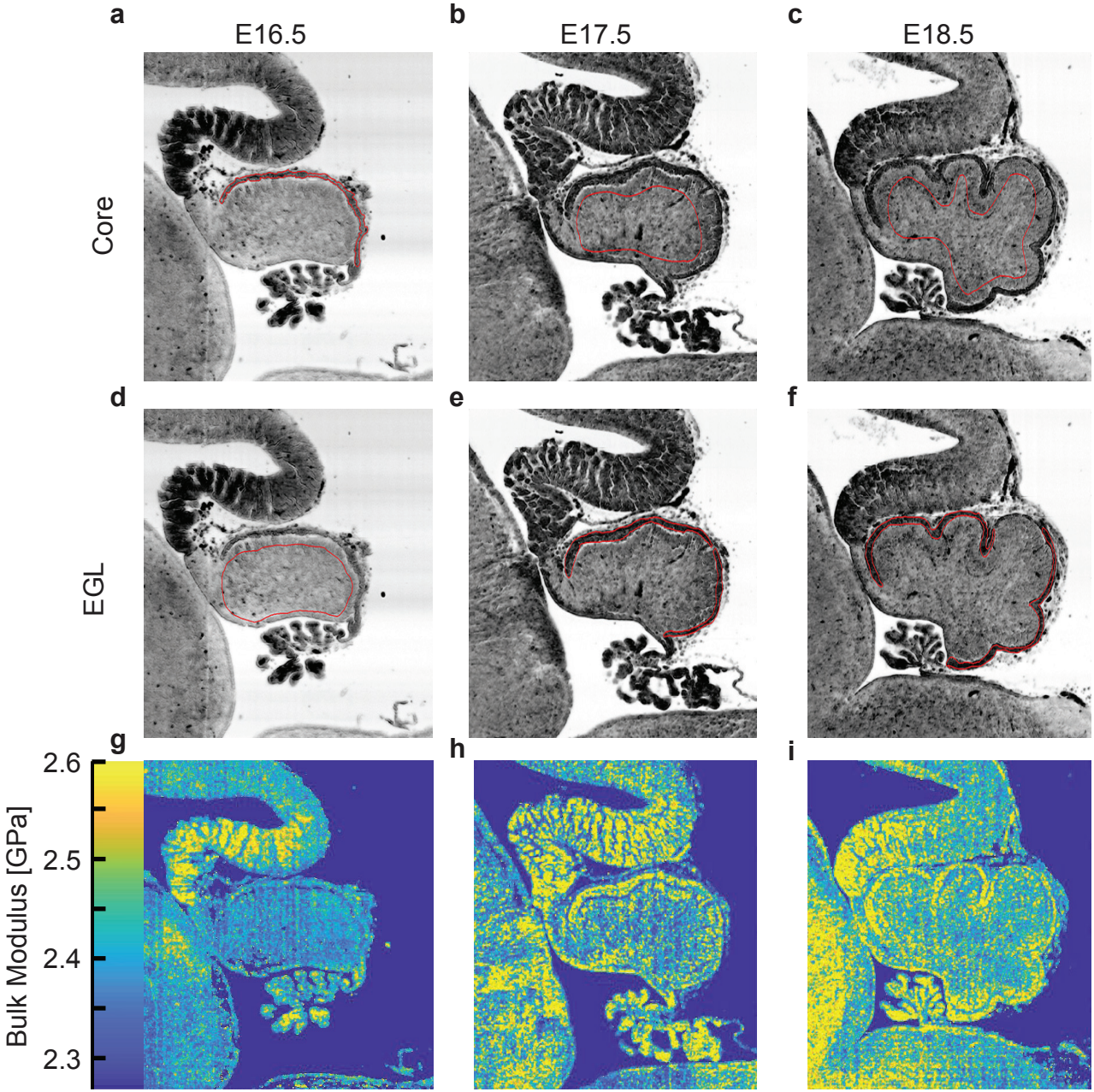

Supplemental Fig. 2: Examples of the regions measured regions by acoustic microscopy. a-f, Examples of the Region of Interest (ROI) measured for each for core and EGL. **h-j**, Representative bulk modulus maps.

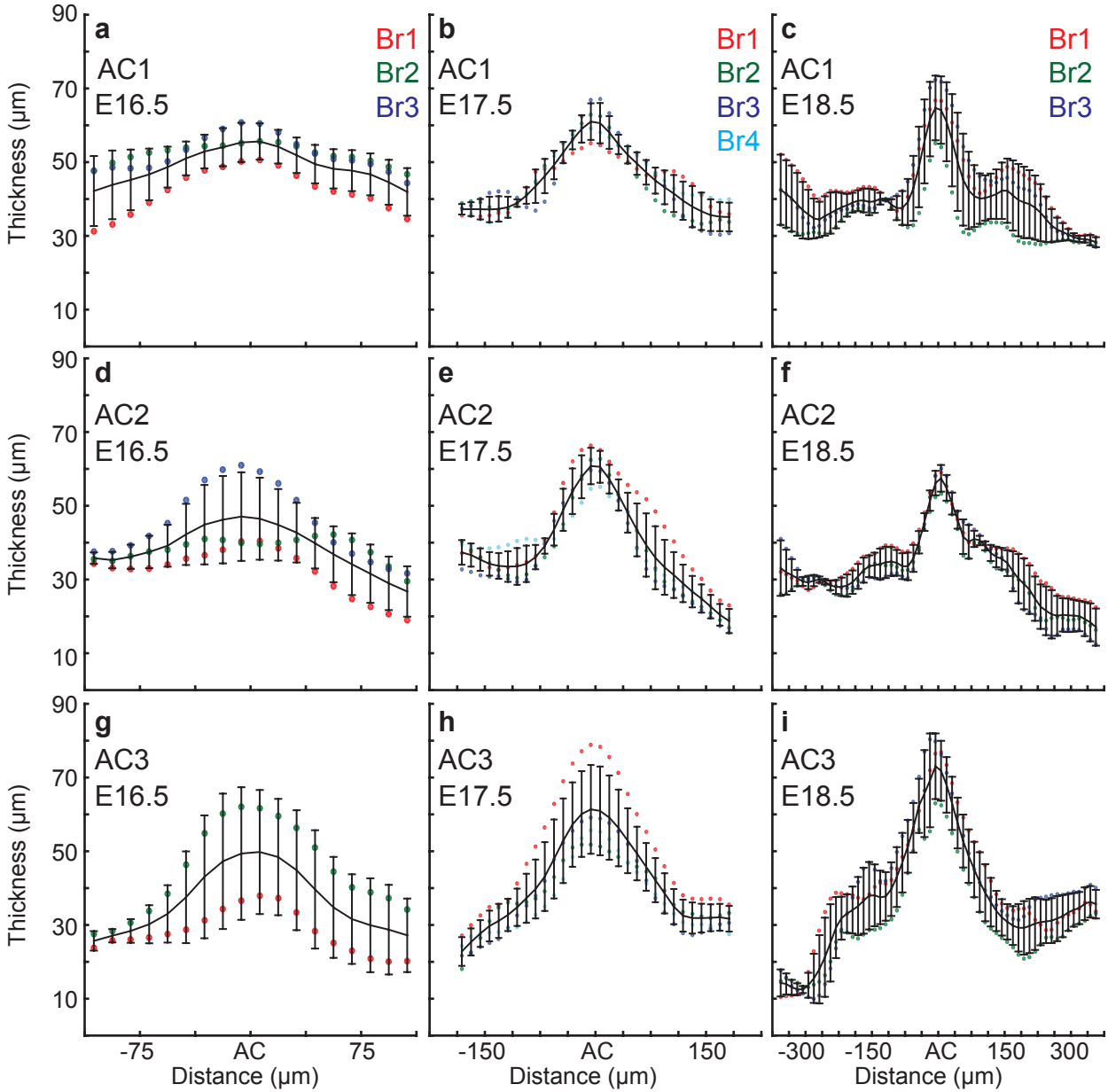

Supplemental Fig 3: EGL thickness increases in the ACs during the initiation of folding. Only E16.5 cerebella that showed regional thickening in the geometry where ACs normally arise were used for the measurements, and one embryo did not yet have an AC3. **a-c**, Thickness variation in and surrounding AC1 (anova **a**, df = 17, P = 0.13, F = 1.55 **b**, df = 29, P = $7.0e^{-14}$ F = 6.82 **c**, df = 57, P = $9.1e^{-11}$ F = 4.05). **d-f**, Thickness variation in and surrounding AC2 (anova **d**, df = 17, P = 0.08 F = 1.74 **e**, df = 29 P = 3.9^{e-22} F = 11.88 **f**, df = 57 P = $2.9e^{-35}$ F = 16.35). **g-i**, Thickness variation in and surrounding AC3 (anova **g**, df = 17, P = 0.59 F = 0.89 **h**, df = 29, P = $2.4e^{-17}$ F = 9.81 **i**, df = 57, P = $7.6e^{-33}$ F = 14.57). Error bars are S.D.

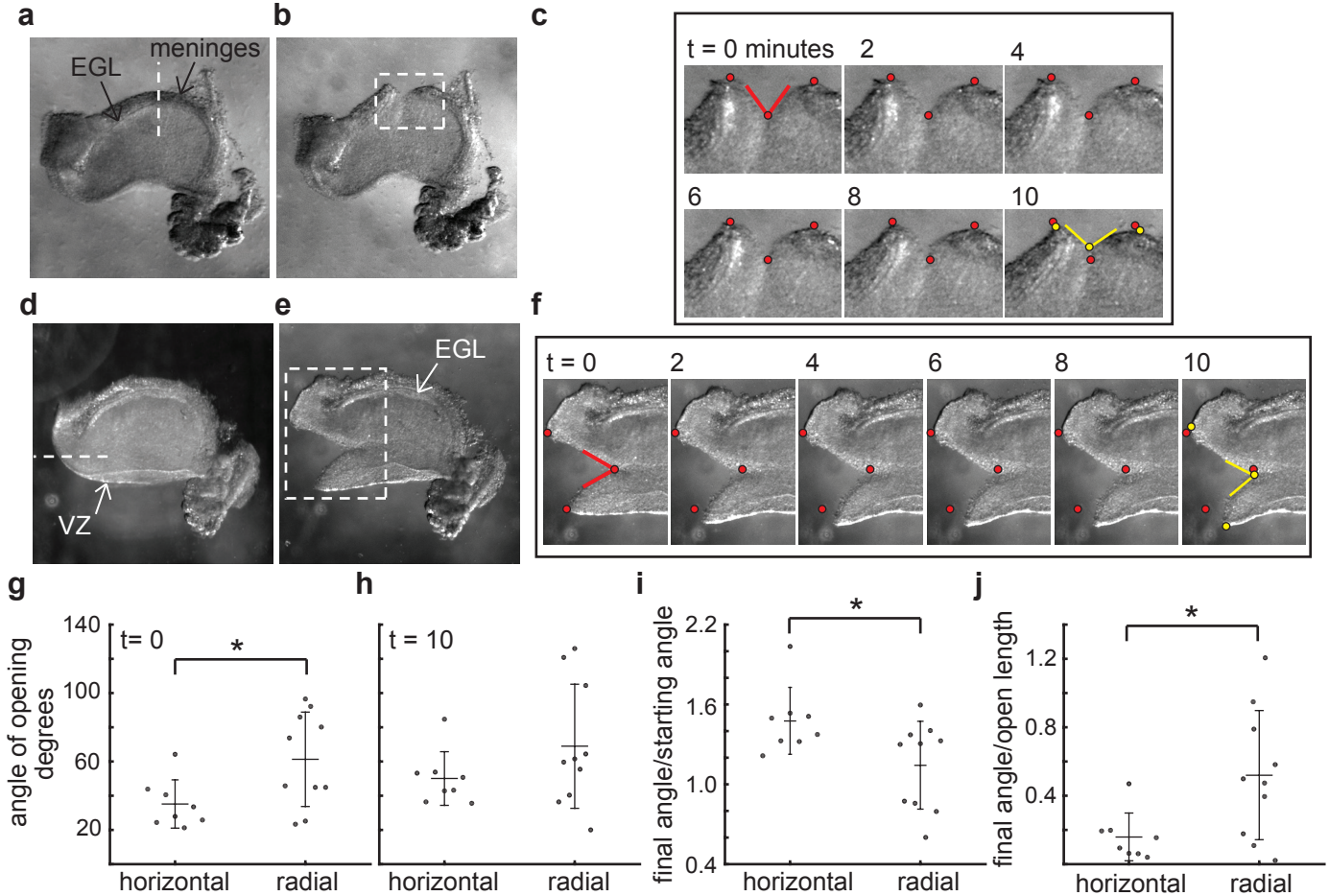

Supplemental Fig. 4: The stress patterns within the cerebellum are different between the EGL and the VZ. a-c, Example of a live cerebellar slice before **a** and after **b** a radial cut through the EGL, and still images from a time-lapse **c**. Time = 0 minutes is at the time it takes to remove the knife and start the imaging, therefore the cut has already begun opening. **d-f**, Example of a live cerebellar slice before **d** and after **e** a horizontal cut through between the EGL and ventricular zone (VZ), and still images from a movie **f**. **g-i**, radial cuts through the EGL open more quickly initially than horizontal cuts between the EGL and the Ventricular zone, but the latter continue to relax for longer (**g**, f-test for unequal varience P = 0.09, two tailed t-test df = 16, p = 0.03, T = -2.43; **h**, f-test P = 0.04 and unequal varience two-tailed t-test df = 12.8 P = 0.16, T = -1.48; **i**, f-test P = 0.49 and two tailed t-test df = 16, P = 0.03, T = 2.43). **j** The degree of opening is tightly related to the length of the opening in horizontal cuts but not in radial cuts (f-test P = 0.02, unequal varience two tailed t-test df = 11.89, P = 0.02, T = -2.80). Stars: statistical differences. Error bars: S.D.

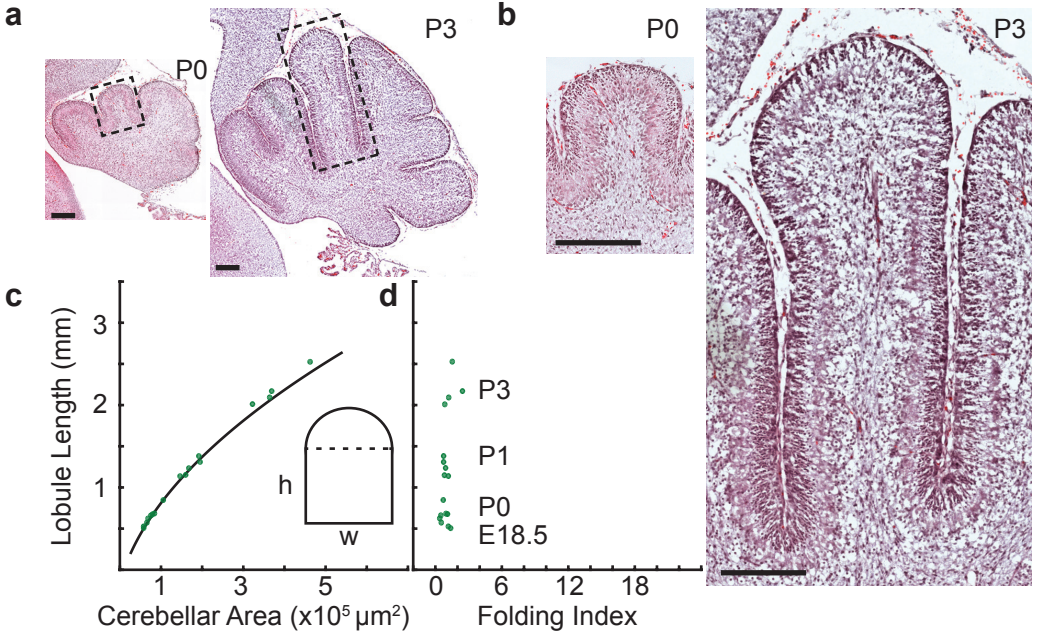

Supplemental Fig. 5: L45 region has a columnar starting shape, proportional expansion, and does not undergo folding from E18.5 to P3. a,b, Low and high power images, respectively, of H&E stained cerebellar sections of FVB/N showing L45 is columnar, whereas L123 and L678 are semi-circular. Scale bar is 200 µm. **c**, Lobule length and area expansion of L45 are proportional to the expansion of a rectangle with a semi-circular top (cartoon). The height of the rectangle expands 5 times as much as the width. **d**, The folding index shows no folding during proportional expansion. Scale Bars: 200 µm

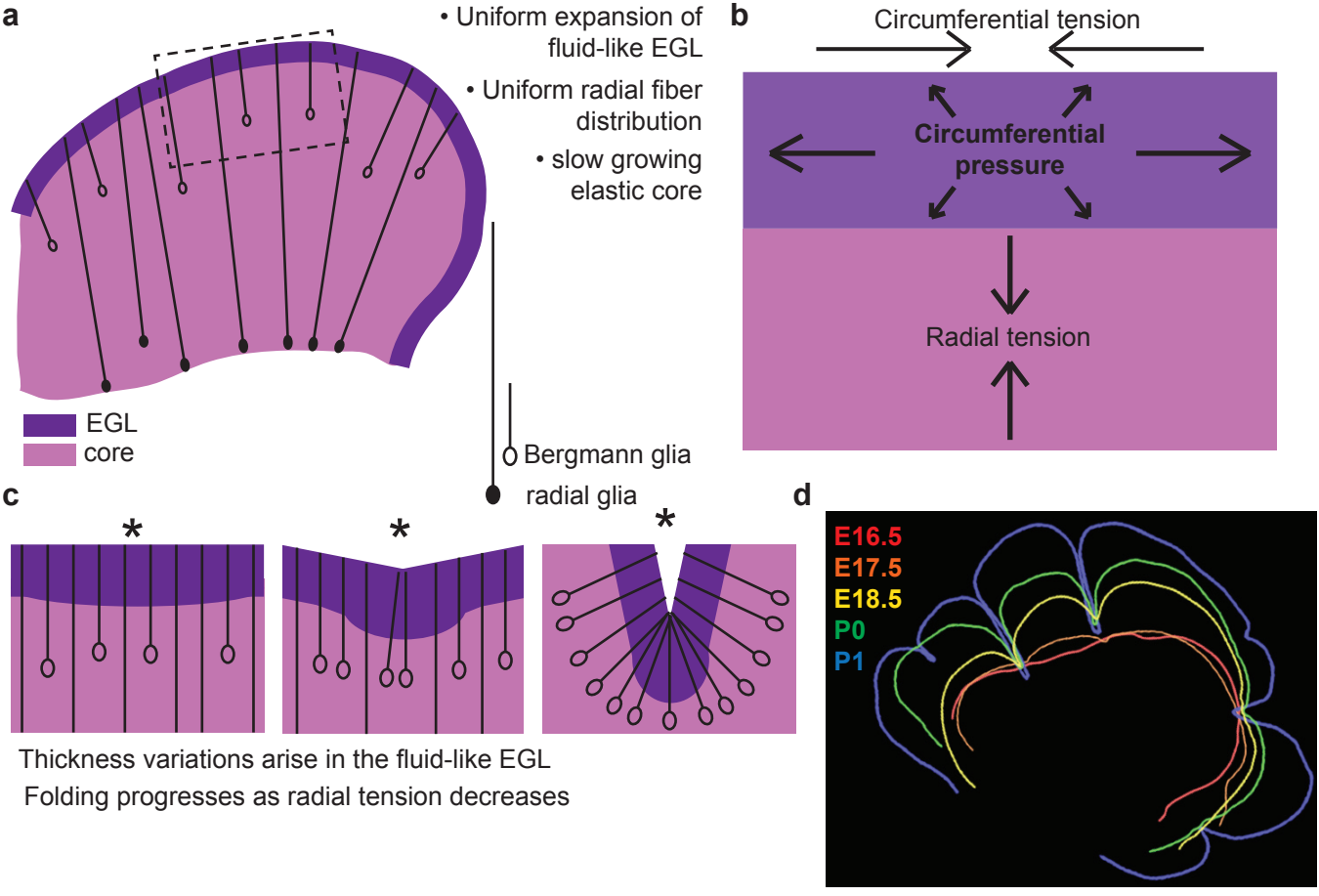

Supplemental Fig. 6: Uniform cell behaviors within a fluid-like EGL create differential expansion based folding approximated by a multiphase model with radial and circumferential tension. a, Cartoon of E16.5 cerebellum showing the EGL (dark purple) overlying the in incompressible core (light purple) with fibers (lines) of radial glia (closed ovals) and Bergmann glia (open ovals) crossing the cerebellum and the EGL. **b**, Map of stress within the cerebellum at the onset of foliation. **c**, Schematics showing that an AC is first detected as a regional inward thickening of the EGL (left). The constraining tensions shape the fluid-like EGL such that the EGL becomes thicker at the AC (middle). As radial glia transition to Bergmann glia, modeling predicts a reduction in radial tension (right). **d**, Since ACs hold their position in space, and compartmentalize the cells within the EGL, we propose that they behave as mechanical boundaries allowing local domains of differential expansion to arise and progressive folding to occur.

Supplementary Movie 1: Live slice cutting and relaxation reveals circumferential tension along the EGL. Time-lapse movie shows relaxation of live tissue slice after cutting radially through the EGL and into the underlying core. Images were acquired every 10 seconds for 10 minutes. The time-lapse was started moments after the tissue was collected in frame after the cut. The slice shown in the video is the same as in Fig. 4f-h.

Supplementary Movie 2: Live slice cutting and relaxation reveals radial tension between the EGL and the VZ. Time-lapse movie shows relaxation of live tissue slice after cutting horizontally into the core between the EGL and the VZ. Images were acquired every 10 seconds for 10 minutes. The time-lapse was started moments after the tissue was collected in frame after the cut. The slice shown in the video is the same as in Fig. 5h-j.